Nanoscale

PAPER

View Article Online
View Journal | View Issue

Cite this: *Nanoscale*, 2025, **17**, 14904

Tuning photophysical properties of semiconducting polymer nanoparticles for improved photocatalytic activity†

Jose Sena-Fernández,[a,b] Esther Rebollar,[c] Aitana Hurtado-Mendoza,[a] Timothy J. Murdoch,[d] Juan Francisco Vega,[a] Ignacio Martín-Fabiani,[d] Tiberio A. Ezquerra[a] and Aurora Nogales *[a]

Received 25th April 2025,
Accepted 30th May 2025

DOI: 10.1039/d5nr01699a

rsc.li/nanoscale

This study investigates the relation between the optical and structural properties of poly(3-hexylthiophene) nanoparticles with their efficiency as photocatalysts for the degradation of water pollutants. Two nanoparticle preparation methods were investigated. Our results indicate that nanoparticles prepared by the miniemulsion method are more efficient in inducing photodegradation. The higher crystallinity, observed by X-ray scattering experiments and the presence of surfactant in these nanoparticles affect the photophysical properties. The fluorescence lifetime of miniemulsion nanoparticles is shorter than that of nanoparticles prepared by the flash method, favoring charge transfer towards the surface of the nanoparticle. These charges, in the presence of water, produce highly reactive oxygen species, responsible for the pollutant photodegradation.

Introduction

Semiconducting polymers have attracted great attention for materials science applications. They can combine the inherent properties of polymer materials (lightness, flexibility, processability, among others) with electrical conductivity and visible light absorption, due to the presence of conjugated π-bonds in the backbone.[1–3] Because of this unique combination of properties, they have been used in organic field effect transistors (OFETs),[4] organic light-emitting diodes (OLEDs),[4] lasers,[5] chemical sensors,[6] and even in therapeutic treatments.[7–9] Of particular interest is the use of semiconducting polymers in organic photovoltaic devices (OPVs),[10,11] where they are used as active materials to convert solar energy into electrical energy. Among the wide variety of semiconducting polymers available nowadays,[12] poly(3-hexylthiophene) (P3HT) is commonly chosen as the model polymer to test and study whether traditional concepts on polymer physics also apply to these functional polymers.[13,14] P3HT has also been used to prove the applicability of semiconducting polymers in advanced applications other than OPVs.[11,15] For example, semiconducting polymers can be used as photocatalysts,[16,17] using light to induce the generation and transport of charges to produce chemical reactions that generate highly reactive oxygen species (ROS).[18–20] Compared to titanium oxide nanoparticles, that are widely used as low cost photocatalysts,[21,22] the large absorption of P3HT in the visible expands its activity as photocatalyst beyond UV range. Besides the applicability of P3HT, this polymer has been deeply studied from a fundamental point of view, therefore constituting an ideal system to correlate changes in physical properties with tunnability in applications. The potential of these highly reactive species to degrade pollutants has boosted research on photocatalysis for environmental applications.[23,24] Water pollution caused by organic dyes widely used in the textile industry has become a problem.[25,26] The demand for clean and safe drinking water is an environmental must be tackled. In the future, lack of access to this clean water could threaten human health and deplete natural or energy resources.[27] Different approaches involving polymeric materials have been taken to tackle the problem of water remediation. Xu *et al.* fabricated bioinspired absorber gels that undergo a phase transition in the presence of clean water, leaving aside the water pollutants.[28] Zhu *et al.*[29] have reported the fabrication of a hybrid Z-scheme photocatalyst with iron nanoparticles (NPs), P3HT and titanium oxide. The ability of semiconducting polymers to produce ROS in the presence of water, enabling them to oxidize or reduce in-

[a]*Instituto de Estructura de la Materia, IEM-CSIC, C/Serrano 121, Madrid 28006, Spain. E-mail: aurora.nogales@csic.es*
[b]*Faculty of Chemistry, Complutense University of Madrid, 28040 Madrid, Spain*
[c]*Instituto de Química Física Blas Cabrera, IQF-CSIC, C/Serrano 119, Madrid 28006, Spain*
[d]*Department of Materials, Loughborough University, LE11 1RJ Loughborough, UK*
† Electronic supplementary information (ESI) available. See DOI: https://doi.org/10.1039/d5nr01699a

organic molecules, has been recently proved.[19] However, there are challenges to be solved before these materials can be deployed in real-world applications. The formation of ROS can degrade the semiconducting polymer itself.[30,31] When considering the use of semiconducting polymers for water treatment, another issue to overcome is solubility. Most semiconducting polymers, including P3HT, are insoluble in water. However, they can be prepared in the form of water dispersible NPs.[32–34] Besides their water dispersibility, processing semiconducting polymers in the form of nanoparticles may enhance their properties compared to bulk materials due to their high surface-to-volume ratio. Also, the photophysical properties of NPs can differ significantly from those of bulk materials. The reduction in particle size can lead to quantum confinement[35] and differences in molecular organization,[33] resulting in unique optical and electronic behavior.[34,36] It has been observed that semiconducting polymer NPs act as efficient light-harvesting agents that transfer the absorbed energy to doped dyes to improve their fluorescence brightness.[37] Lifetimes of the different processes that take place following light absorption by semiconducting polymers depend on factors such as morphology,[38] crystalline structure, and chemical environment.[39] Various competing processes have been identified, such as radiative emission, non-radiative relaxation processes such as charge transfer, and intermolecular interactions such as exciton–exciton interactions.[36,39] Understanding the role of each of these processes is critical because excited state deactivation mechanisms can be key to ROS generation.

In this work, we investigate the properties of P3HT NPs prepared by different methods, focusing on the photophysical properties, including their absorption/emission spectra and fluorescence lifetimes. We correlate these results with the NPs efficiency to photodegrade a model organic water pollutant. Our results show that tuning the physical properties of the semiconducting polymer NPs enhances their potential in environmental and catalytic applications. This could open new avenues for the development of more efficient water remediation technologies.

Experimental

Materials

The P3HT sample with 97.6% regioregularity, 60.15 kDa weight average molecular weight and a polydispersity index of 2.1 was supplied by Ossila (Batch number M1011). The polymer was used without further purification. Different solvents were used for different types of NP preparations described below. Tetrahydrofurane (THF) (EMPARTA ACS, purity >99.5%, Merck, Darmstadt, Germany) and chloroform ($ClCH_3$) (purity >99.98%, Quimipur SLU, Madrid, Spain) were used. In some preparations, sodium dodecyl sulfate (SDS, from Sigma Aldrich, ACS reagent grade, St Louis, MO, USA) was used as a surfactant. The excess of surfactant was removed by dialysis using a dialysis tubing membrane (Visking DTV, Medicell Int Ltd London, UK). The cutoff range was 12 000–14 000 g mol^{-1} and the tube diameter was 25.5 mm. Methylene blue (methylthioninium chloride, supplied by Merck, purity ≥82%, M_w 319.85 g mol^{-1}, powder) was used as a model dye for photodegradation experiments.

Preparation of the nanoparticles

Flash nanoprecipitation. For this preparation method, the polymer was dissolved in a water-miscible solvent. In the present case, THF (boiling point of 66 °C) was used. A given volume of the polymer solution was mixed with a given water volume using a syringe and stirred energetically for 15 minutes to induce solvent displacement. Finally, the mixture was heated and gently stirred to evaporate the solvent. NPs from different solution concentrations and different solvent/water ratios were prepared. The optimum conditions in terms of minimizing particle aggregation and maximizing NP yield were observed for the sample prepared from 3 g L^{-1} solution and solvent water volume ratio 1/6.

Miniemulsion. To obtain P3HT NPs through the miniemulsion method, a 3 g L^{-1} P3HT solution in $CHCl_3$ (boiling point of 62 °C) was prepared and heated at 40 °C for 1 h. Then, the polymer solution was mixed with the same volume of 1 wt% SDS solution in water. An emulsion was formed by stirring vigorously for two hours at room temperature. Then, a miniemulsion was obtained by ultrasonication for 15 min, using an ultrasonic bath (power = 480 W) at room temperature. To evaporate the $CHCl_3$, the mixture was heated to 70 °C under continuous gentle stirring for 3 hours. Excess SDS was removed by dialyzing against distilled water for 2 days, with several water exchanges, after four hours in the first eight hours and an additional exchange on the second day.

Characterization techniques

Atomic force microscopy (AFM). Atomic force microscope data were recorded for P3HT surfaces on SiO_x wafers attached to metallic sample holders using a Multimode 8 controlled with Nanoscope V software (Bruker, Karlsruhe, Germany). Topographic AFM images were taken in tapping mode, using gold-coated silicon probes (Tap300GB-Gprobes, BudgetSensors, Sofia, Bulgaria) (resonant frequencies = 300 kHz, k = 40 N m^{-1}). P3HT NPs were deposited under ambient conditions onto conductive As doped n-type silicon wafers (resistivity < 0.005 Ω cm) (⟨100⟩, Neyco, both sides polished). The deposition was performed either by spin coating at 3000 rpm during 2 minutes or by drop casting. The wafers were cut into square slides with dimensions of 2 cm × 2 cm, cleaned in an ultrasonic bath with acetone, then isopropanol for 10 min each, and then dried with a N_2 stream. The P3HT dispersions were ultrasonicated for 5 min and stirred before deposition to obtain a uniform mixture. The sample was fixed with adhesive tape to an iron support. Image processing and NPs size analysis were performed with NanoScope Analysis 1.50 software (Bruker).

Dynamic light scattering. DLS size measurements were performed in water dispersions of the NPs with a Zetasizer Nano ZS instrument (Malvern Instruments, Worcestershire, UK). An

internal control of the instrument was performed with distilled water before each measurement to ensure that no signals were present in the correlogram. Disposable cuvettes (2.5 mL, BrandTech) were used to perform the measurements. The Nano ZS instrument incorporates non-invasive backscattering optics (NIBS) and homodyne detection to avoid artefacts in particle size determination. The sample was illuminated with a λ_0 = 633 nm laser at constant power and the intensity of the scattered light was measured at an angle of θ = 173° using an avalanche photodiode. Measurements were performed at a temperature of 25 °C, with the samples previously sonicated to eliminate any aggregates that might have formed. Three acquisitions per sample were performed with multiple runs to obtain an average size. Data were processed using the SEDFIT program[40] to overcome the shortcomings of traditional linear fitting for polydisperse samples. Cumulant analysis was used to obtain size and polydispersity, and the number of populations was obtained by second derivative analysis.

Wide-angle X-ray scattering (WAXS). Wide-angle X-ray scattering in grazing incidence geometry (GIWAXS) experiments were performed at the NCD-SWEET beamline of ALBA Synchrotron (Cerdanyola del Vallès, Barcelona, Spain). An X-ray wavelength was set at λ = 0.1 nm (E = 12.4 keV) using a Si (111) channel-cut monochromator. The beam size at the sample position was 30 × 120 μm^2 (vertical × horizontal). The incidence angle for the X-rays was 0.2°. WAXS patterns were recorded with an LX255-HS detector from Rayonix located at 0.152 m from the sample position. WAXS patterns, acquired with an acquisition time of 5 s, were corrected from background scattering and azimuthally integrated using PyFAI software.[41] In both cases the scattering intensity is represented as a function of the module of the scattering vector $q = 4\pi(\sin\theta)/\lambda$, where 2θ is the scattering angle. Azimuthal integration on the 2D images led to 1D scattering patterns, which are presented in this work after background subtraction. The dispersion of NPs in water was drop-cast onto a silicon wafer and allowed to dry for several days.

Optical characterization. *UV-Vis*: optical absorption experiments in the visible and ultraviolet range of the spectrum were recorded by using a UV-3600 Shimadzu spectrophotometer (Duisburg, Germany), which was controlled using LabSolutions UV-Vis control software. NP suspensions were poured into quartz cuvettes with 5 mm path lengths (100QS, HELLMA Analytics, LineaLab). *Photoluminescence (PL)*: emission spectra obtained from photoluminescence experiments were performed with a FluoroMax 4 spectrofluorometer (HORIBA Jovin Yvon) using an excitation wavelength of 555 nm. For PL polystyrene cuvettes of 1 cm length path in the case of aqueous dispersions were used (Brand, Wertheim, Germany). Fluorescence Lifetime Imaging Microscopy (FLIM) measurements were performed on a Micro Time 200 confocal microscope (PicoQuant, Berlin, Germany) integrated with an IX73 inverted microscope (Olympus, Hamburg, Germany). The excitation was produced with a diode laser (LDH-D-C-640, PicoQuant, Germany) at an emission wavelength of 640 nm by a PDL-828 pulsed laser diode driver (PicoQuant, Germany). The pulse width was approximately 0.7 ns (IRF FWHM) and a 25 ns repetition window between each pulse. Excitation light was passed through a dichroic mirror (NFD01-532, Semrock, Rochester, USA) and then coupled into a single-mode fiber. This light was focused through either a PLN20×/NA 0.4 or PLN10×/NA 0.25 lens (Olympus) depending on sample thickness. Fluorescence emission was collected using the same objective and was separated from the excitation light using a dichroic mirror (ZT532/640 rpc-UF3, Chroma, Bellows Falls, USA). The separated light then passed through a tube lens, 50 μm pinhole and 690/70 BP filter (AHF, Germany) onto a hybrid photomultiplier detector (PMA-hybrid-40, PicoQuant). The detector is connected to a time-correlated single photon-counting (TCSPC) device (Hydraharp400, PicoQuant) to collect time-tagged data from the laser and detector. The TCSPC technique generates time-, space- and spectrum-resolved fluorescence decay data sets.

Fluorescence decay lifetimes were obtained by fitting the curves with four exponential decays convoluted with the instrument response function IRF and considering a background (eqn (1)).

$$I(t) = b + \mathrm{IRF} \times \sum_i a_i e^{-\frac{t}{\tau_i}} \quad (1)$$

The analysis allowed extraction of representative lifetimes (τ_i) and amplitudes (a_i) of the different decay components.

All samples were measured without any specific pretreatment. Dried nanoparticle suspensions were measured on 0.16–0.19 mm thick coverslips and films were measured on glass slides. The samples were covered so that no external light interfered with the measurements.

Photodegradation tests

A volume of 0.1 mL of NP suspensions with a concentration of P3HT of 0.5 g L^{-1} was mixed with 1 mL of a solution of MB in water (15 mg L^{-1}). The mixture was poured into a quartz cuvette (100QS, HELLMA Analytics, LineaLab) of 5 mm path length. In this way, UV-VIS experiments to estimate the MB content were performed in the same volume exposed to the lamp light, without the need of extracting aliquots each time. Then it was exposed to a EQ-99X LDLS lamp (Energetiq Technology) located at a distance of 70 cm. The samples were thermostatized at 30 °C during the irradiation time. In each experiment, a control cuvette containing the MB solution without P3HT NPs was also irradiated. Before the photocatalytic degradation experiment, the suspension of MB and the P3HT NPs used as photocatalyst was magnetically stirred in the dark for 30 min to achieve adsorption equilibrium. At the given irradiation time, the samples were studied using the UV–Vis spectrophotometer. The photodegradation efficiency was determined by calculating the MB concentration at a given irradiation time through the UV-Vis absorption peak maximum of MB located at 664 nm, using the Lambert–Beer law (eqn (2)):

$$A_{664} = \varepsilon_{664} \cdot c \cdot l \quad (2)$$

where A_{664} is the absorbance measured at 664 nm, ε_{664} absorption coefficient of MB, with a value of 0.194 mg^{-1} L cm^{-1}, c is the concentration in mg $L^{-1}$and l is the path length in cm (see Fig. S2 ESI†).

The degradation efficiency $\chi(t)$ can be calculated as:

$$\chi(t) = 100\frac{C_0 - C(t)}{C_0}, \quad (3)$$

with C_0 being the initial MB concentration of the solution, and $C(t)$ the concentration at a given exposure time.

Liquid chromatography-mass spectrometry (LC-MS). For the analysis of the dye degradation products, they were separated by using a HyPurity C18 column (100 mm × 2.1 mm, 3 μm particle size, Thermo Fisher Scientific) at a flow rate of 0.2 mL min^{-1}. Before analysis the samples were centrifuged for 1 minute at 12 000 rpm, diluted in Milli-Q water to 1/10 and filtered.

A gradient consisting of water (eluent A), acetonitrile (eluent B), and HCOOH 5% (eluent C) was used. The elution program started with 2 min isocratic conditions (88% A; 10% B; 2% C), and then the percentage of B was increased to 90% in 10 min, maintaining constant the 2% of eluent C, and consequently, decreasing the percentage of eluent A. These final conditions were kept for 10 min. An injection volume of 100 μL was set for all LC analyses. Detection was done in the electrospray ionization mode. Bruker Compass 1.2 software was employed for LC-MS/MS data acquisition and processing.

Results and discussion

Morphology of the P3HT nanoparticles

Flash and miniemulsion methods produced NPs with a clear tendency toward spherical morphology and very similar sizes as measured by AFM (Fig. 1a and b). Quantitative analysis of the size distribution was performed in several regions of spin coated silicon wafers. The distribution of sizes includes NPs with diameters ranging between 10 nm to 100 nm in both cases, with the higher frequency of diameters around 20 to 30 nm (Fig. 1c). However, the distribution of miniemulsion NPs shows a bimodal shape, with a narrow peak around 20–30 nm in diameter and a broader one around 60 nm. For the case of flash NPs, the distribution is broader and centered around 30 nm.

DLS measurements were also performed on the NP water suspensions. The results obtained in terms of diameter by number and polydispersity compared with AFM measurements, are presented in Table 1. Additional details regarding the DLS protocol are included in the ESI.† DLS measurements show larger diameters compared to AFM, with a more significant discrepancy observed for miniemulsion NPs. This difference may be attributed to variations in the hydrodynamic radius between the two types of NPs. Specifically, miniemulsion NPs are stabilized by surfactant molecules, which may influence the dynamics of the NPs in water. In addition, unlike flash NPs, the polydispersity of miniemulsion nanoparticles is found to be negligible in DLS measurements, probably due to the presence of two populations of NPs, one of them with sizes beyond that recorded by the DLS instrument.

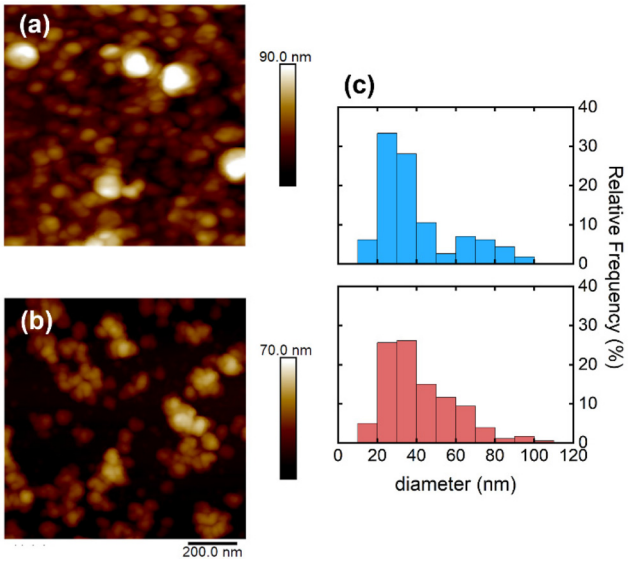

Fig. 1 AFM topography images of P3HT NPs deposited on a silicon wafer. (a) Miniemulsion NPs and (b) flash NPs. (c) Particle size histograms for miniemulsion NPs (blue histogram) and flash NPs (red histogram).

Table 1 Mean diameters (in nm) and polydispersity values for P3HT nanoparticles, as determined by AFM and DLS

	AFM	DLS	
	Diameter (nm)	Diameter (nm)	Polydispersity
Flash	42 ± 19	54 ± 7	$0.13 \pm 1.6 \times 10^{-2}$
Miniemulsion	40 ± 20	86 ± 2	$4.7 \times 10^{-2} \pm 3.5 \times 10^{-3}$

Crystalline structure of the NPS prepared by miniemulsion and flash methods

WAXS experiments (Fig. 2) of both types of particles show the characteristic features of the form I crystalline phase of P3HT: an intense diffraction maximum at q = 3.8 nm^{-1} (100), corresponding to the stacking of the main chain/side chain layered structure of the P3HT crystal, with its second-order (200) and third-order (300) diffractions peaks also visible at 7.6 nm^{-1} and 11.4 nm^{-1}.

The third order is more evident in the case of miniemulsion NPs, indicating a higher degree of crystallinity. It has been reported that the affinity between dodecyl chains of SDS and hexyl chains of P3HT may produce a mixed supramolecular phase between P3HT and SDS, resulting in some modifications in the crystalline structure.[34] WAXS results support also this observation. The WAXS curves obtained from each type of NPs have been analysed to obtain the dimensions of the unit cell and the fraction of crystallinity. The protocol for

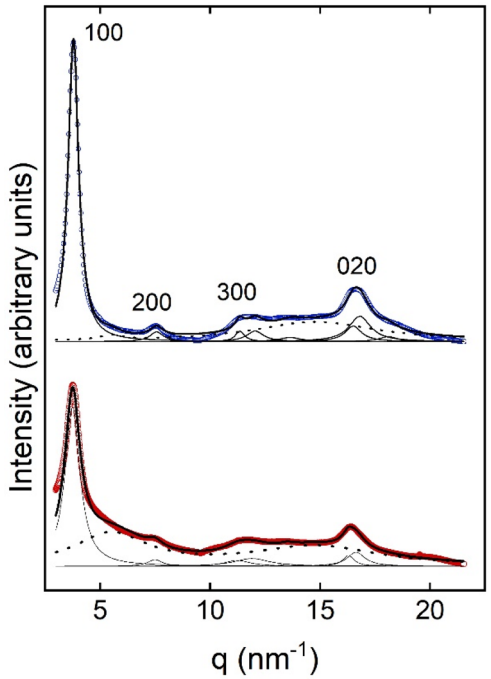

Fig. 2 WAXS intensity of PH3T miniemulsion NPs (blue) and flash NPs (red) deposited on a silicon wafer. Thick black lines correspond to the best fit to the simulated two phase model considering the monoclinic crystalline structure and the amorphous fraction. Thin black lines correspond to the individual Bragg reflections, and dotted line represents the amorphous halo. Further details are included in the ESI.†

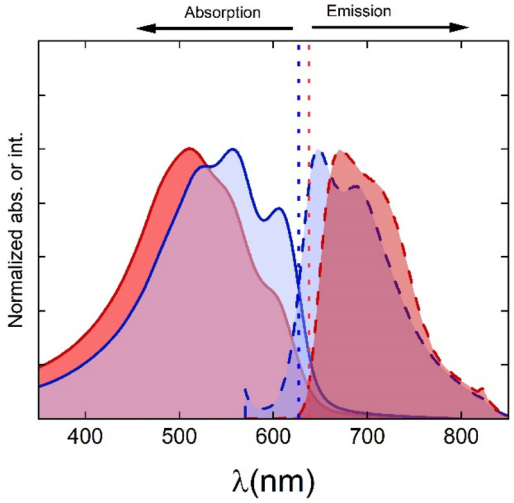

Fig. 3 Absorption (UV-Vis) and emission (photoluminiscence) spectra of flash P3HT NPs (red) and miniemulsion P3HT NPs (blue). Excitation wavelength 555 nm. The curves were normalized to the maximum intensity.

deconvoluting the WAXS data considering the amorphous and crystalline contributions is described in the ESI.† The dimensions of the unit cell for each case and the fraction of crystallinity for each type of NPs are presented in Table S1.† The obtained results show that the unit cell of crystals in miniemulsion NPs has a lower volume than that of flash NPs, indicating a more compact arrangement of the chains in the case of miniemulsion NPs due to increased lamellar stacking. Also, miniemulsion NPs present higher crystallinity and larger crystalline sizes.

Optical properties of the P3HT nanoparticle suspensions

The NP preparation method significantly impacts on the optical properties of the water suspensions. Fig. 3 shows the absorption and emission spectra of water suspensions of P3HT NPs prepared by flash or miniemulsion method. For the case of miniemulsion, the UV-Vis absorption presents three clear maxima, located at 525 nm, 556 nm, and 607 nm, which are associated with the π–π* electronic transitions to different vibronic levels (2–0, 1–0 and 0–0 transitions, respectively).[42] The 0–0 and 1–0 transition is also well defined in the emission spectra. The absorption spectra for miniemulsion NPs, shows a ratio A_{0-0}/A_{0-1} is 0.8, whereas for flash NPs this ratio is around 0.6. According to the description in terms of H- and J-aggregates proposed by Spano *et al.*[43] a higher A_{0-0}/A_{0-1} ratio corresponds to a higher level of intra-chain order and planarization of the P3HT chains, which is characteristic for J-aggregates. Other signatures of the presence of J-aggregates include the shift towards higher wavelengths of the absorption spectra and the enhancement of 0–0 transition. The absence of well-defined peaks in the optical spectrum for flash-derived NPs suggests lower crystallinity than that of miniemulsion NPs, in agreement with the X ray results. To corroborate this, the absorption spectra were analysed using the modified Frank Condon approximation (see ESI, Fig. S3†). From this analysis, the 0–0 vibronic transition appears at lower energies (E_0) for miniemulsion NPs than for flash NPs. Also, the free exciton bandwidth is considerably lower for miniemulsion NPs than for flash NPs (see Tables S2 and S3 of the ESI†). Both aspects are related to a higher planarization of the chains in the aggregates.[43] The Frank Condon analysis allows also to estimate the fraction of aggregates in the NPs, resulting in 73% for the miniemulsion process and 60% for the flash NPs, which is qualitatively in agreement with the crystallinity obtained by X ray diffraction.

Optical and X ray results suggest that the packing of the chains is less efficient in the case of flash NPs, and therefore, a larger band gap should be expected. Analysis of both absorption spectra by construction of a Tauc plot[44] yields similar values for the band gap of both types of NPs, although slightly smaller for miniemulsion NPs (1.95 eV for miniemulsion NPs and 1.97 eV for flash NPs). Tauc plots for both types of NPs are presented in the ESI (Fig. S4†).

However, the bandwidth in the case of miniemulsion NPs is considerably smaller than the one obtained for flash NPs, indicating that in flash NPs, there is a higher chain torsional disorder. To understand the differences observed in optical properties and their relationship with the way the excitation energy flows in the NPs prepared by the different methods, fluorescence lifetime experiments were performed. Fig. 4a shows the fluorescence signal decay after excitation at 640 nm

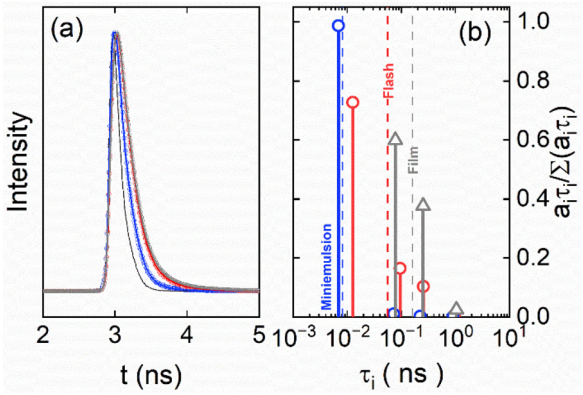

Fig. 4 (a) Fluorescence decays of P3HT NPs prepared by flash technique (red symbols), miniemulsion technique (blue symbols), and thin film (grey symbols) following excitation at 667 nm. The continuous thick lines correspond to fits with four exponential terms in the case of the NPs and three exponential terms for the thin film. The thin black line represents the IRF of the instrument. (b) Resulting decay times (τ_i) and normalized intensities considering the preexponential coefficients (a_i), for the three studied systems. Same color code as in (a). Dashed lines show the intensity-averaged lifetimes obtained from the fits.

for flash NPs and miniemulsion NPs, respectively. The fluorescence decay for a control P3HT film of around 300 nm in thickness is also presented.

Depending on the system, different number of exponential functions were needed to fit the fluorescence decay curves. The obtained decay times can be grouped in four regions: 10^{-2} ns time scale, two characteristic times around 10^{-1} ns and 2×10^{-1} ns, and some longer times around the 1 ns timescale. We will refer to these times as τ_4, τ_3, τ_2, and τ_1 respectively, following the notation by Ferreira *et al.*[45] The intensity weighted contribution of each of these decay times is different for each system. Fig. 4b shows the weight of each of the exponential decay as a function of the characteristic decay time for the three systems studied. More details of the fitting parameters are shown in the ESI (Fig. S5 and Tables S4, S5†).

In the P3HT thin film, the shortest lifetime τ_4 is absent, and the decay process can be described with contributions of τ_3 and τ_2, along with a lower amplitude contribution from the process with characteristic time τ_1. These results agree with those observed by other groups.[39,46,47] However, for the two types of NPs, the shortest time τ_4 is the main component. According to the literature τ_4 is associated with the transition from a hot photoexcited state to a geometrically relaxed aggregate state.[39] Gosh *et al.* have suggested that, in P3HT NPs in aqueous media, most of the hydrophobic polymer chain coil together.[36] In the case of miniemulsion NPs, this hydrophobic–hydrophilic arrangement is enhanced by the presence of the SDS surfactant. In these circumstances, chromophores responsible for the fluorescence are closer to each other than in the case of P3HT thin film, and therefore a higher proportion of aggregates responsible for this transition is expected. The decay characteristic times τ_3, τ_2 and τ_1 observed both in the thin film and flash NPs have been assigned in the literature to the decay of emissive states in P3HT,[47] which is consistent with a high density of crystalline aggregates in the material. These states may correspond to excitons confined in crystalline regions, excitons localized in defects or charge-transferred excitons.

When comparing both types of NPs, the main component miniemulsion NPs show only the decay related to the hopping transition to lower energy sites with a conformational planarization of the polymer backbone.[46,48] On the contrary, flash NPs exhibit some contributions from decay of emissive states due to exciton recombination, which is consistent with lower crystallinity and higher structural disorder. This structural disorder can limit the efficiency of controlled energy transitions, resulting in a red shift in emission properties (Fig. 3). The absorbed energy in the case of miniemulsion NPs should be dissipated then by other means. The higher efficiency of charge transfer in the miniemulsion would explain the lower weight of τ_3, τ_2 and τ_1 in their fluorescence decay. The reversible formation of a charge transfer complex between polymer and molecular oxygen has been reported in the presence of water.[49] This formation is enhanced under visible light illumination. It has been reported that, in electrolyte solutions, P3HT can be polarized by the water environment, lowering the polymer energy levels. Photogenerated electrons are then preferentially localized at the polymer–water interface.[50] In miniemulsion P3HT NPs, this effect is further enhanced by the promotion of photogenerated electrons from the inner P3HT core to the outer hydrophilic regions, leading to higher reactivity with the environment. Therefore, photocatalytic differences due to the formation of reactive oxygen species by the two types of NPs in the presence of water could be expected. In the following section, we investigate whether these differences affect the application of the NPs in the photodegradation of water contaminants.

Methylene blue degradation by the presence of P3HT NPs

To prove this idea, photodegradation tests were conducted on water solutions of MB. Fig. 5a and b show UV-Vis spectra of MB solutions exposed to light for different durations in the presence of flash and miniemulsion P3HT NPs. MB solution spectra show an intense peak centered around 664 nm, which is used to estimate the concentration of the studied solutions following eqn (2).

The degradation efficiency as a function of exposure time is presented in Fig. 5c in MB solutions in the presence of both types of P3HT NPs. For comparison, the efficiency of MB degradation only by light exposure is also presented.

To ensure that the MB is being degraded by the action of light and that the color decrease observed is not due to MB adsorption on the NPs surface or to the formation of uncoloured derivatives as leuco methylene blue or oxidised methylene blue[51] we performed LC-MS analysis of the samples after 240 min irradiation and results are shown in Fig. S6.† Initial LC-MS profile of MB shows a prominent peak at a time of 12.8 min corresponding to m/z 284.2 and assigned to MB molecule. Additional peaks at m/z 270.2 and m/z 227.2 are assigned to azure B and thionin, compounds with one and

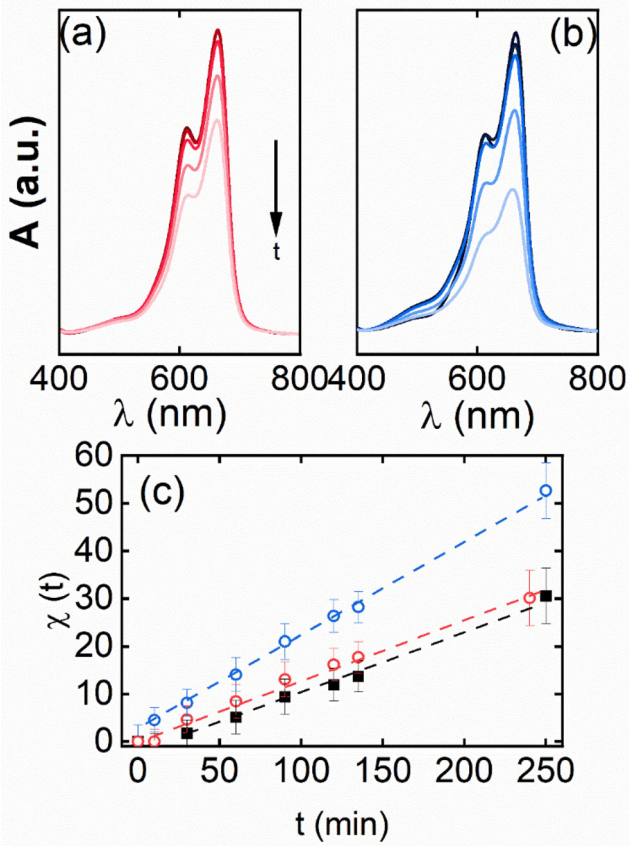

Fig. 5 MB solution UV-VIS spectra obtained after light exposure for 0, 10, 30, 120 and 240 min in the presence of flash P3HT NPs (a) and miniemulsion NPs (b). In (c) degradation efficiency, $\chi(t)$, as a function of the irradiation time in the presence of miniemulsion NPs (blue symbols) and flash NPs (red symbols) is plotted. For comparison, black symbols show the degradation of MB by the solely action of light.

three fewer methyl groups than MB respectively (see Fig. S7†). When MB alone is exposed to light for 240 min, the MB peak intensity decreases and the intensity of the peak assigned to thionin increases, indicating demethylation cleavage as previously reported in literature.[52] In the case of light irradiation of the solutions containing P3HT NPs, the MB peak has disappeared and also the intensity assigned to thionin has significantly decreased, which indicates the almost complete degradation of MB. In addition to the LC-MS analysis of the solutions, the pH was measured initially and after light exposure, and a decrease was observed, which would be in agreement with the mineralisation of MB and the formation of acid species which contribute to the pH reduction.[53]

Regarding the degradation efficiency, as observed in Fig. 5, there is a clear enhancement when P3HT NPs are present. This effect is stronger in the case of miniemulsion NPs. This result can be correlated with a smaller gap value in this case, increasing the generation of photoexcited electrons. In addition, SDS improves the crystallinity and conformational planarization of the NPs, but may also modify the NP–water interface, facilitating the degradation of MB through increased electron transfer.

The higher crystallinity in the NPs prepared by miniemulsion, confirmed by X-ray, also can favour charge mobility and separation and reduces unwanted exciton recombination and minimise non-radiative losses, thereby facilitating the formation of reactive oxygen species at the NP–water interface is then more efficient for miniemulsion NPs, improving the degradation of MB. In these NPs, our results show that the absorbed energy from light is not dissipated as fluorescence (Fig. 4a), and it appears to be redirected to charge transfer processes, which directly correlates with the higher efficiency of MB photodegradation. The fluorescence decay of the miniemulsion NPs highlights a dominant contribution from charge transfer-related processes (τ_4), such as jump transitions to lower-energy sites, either more ordered or less energetic regions. This is because short-lived excitons, which have a greater weight, are likely involved in non-radiative processes that precede the energy conversion into fluorescence. In contrast, in flash-prepared NPs, the greater structural disorder hinders charge separation, leading to exciton recombination and lower photocatalytic performance.

Conclusions

This study highlights the importance of controlling the internal structural, optical, and functional properties of P3HT NPs to optimize their photocatalytic activity through the preparation method.

Fluorescence lifetimes of P3HT prepared in the form of NPs by miniemulsion and flash techniques, as well as in thin films, revealed fundamental differences in the decay processes and provided insight into the de-excitation events. The analysis of the fluorescence lifetimes suggests that the deactivation of the excited state in miniemulsion NPs occurs mainly by exciton transition to lower energy states and conformational planarization of the polymer backbone. Meanwhile, flash NPs showed additional contributions from the decay of emissive states due to exciton recombination, similar to what it is observed in P3HT thin films.

Structurally, the miniemulsion NPs were characterized by higher and more homogeneous size and also higher crystallinity, as confirmed by AFM, DLS and X ray diffraction. These observed differences are attributed to the presence of surfactant in miniemulsion NPs. The optical properties of miniemulsion NPs reveal a smaller band gap and more defined bands. The higher crystallinity and surfactant-induced planarity in the miniemulsion NPs could explain these optical properties, which enhance their photodegradation efficiency. The higher crystallinity facilitates charge transfer, a non-radiative process that competes with fluorescence and is associated with the generation of free radicals involved in photodegradation. The flash prepared NPs, on the other hand, show lower band resolution and a red shift that could be due to lower structural organization, resulting in a higher contribution of radiative processes and a lower photodegradation efficiency.

Author contributions

J. S. and A. N. initiated this work. A. N. supervised the method of nanoparticle preparation. A. H. M. carried out the experiments to obtain the absorption coefficient for the contaminant. J. S. and E. R. emission experiments. J. S. performed the AFM and UV-Vis characterization, supervised by A. N. and E. R. J. S., A. H. M. and J. F. V. performed and analysed the DLS experiments. J. S., T. J. M. and I. M. F. performed the FLIM experiments, and together with A. N. analysed them. J. S., E. R., A. N. and T. A. E. performed and analysed the WAXS experiments. J. S. and A. N. wrote the first manuscript with contributions from all authors. A. N. reviewed the final version of the manuscript. All authors participated in the discussion of the results commented on the manuscript.

Data availability

The data that support the findings of this study are available from the corresponding author upon reasonable request.

Conflicts of interest

There are no conflicts to declare.

Acknowledgements

This work was supported by grants PID2019-107514GB-I00, PID2022-138635NB-I00 funded by MCIN/AEI/10.13039/501100011033, by grants TED2021-131914B-I00 and TED2021-129845B-I00 funded by MCIN/AEI/10.13039/501100011033 and by "ERDF A way of making Europe". JS acknowledge the funding by MCIN/AEI/10.13039/501100011033 through grant number PRE2020-094362 and by the Regional Government of Madrid through the project TEC MATRIX-CM (TEC-2024/TEC-85). The support from the Scientific Network on Photocatalysis OASIS funded by the Consejo Superior de Investigaciones Científicas (CSIC), Spain is also acknowledged. AHM acknowledges funding by the JAE program, CSIC. The authors acknowledge M. Malfois for support in the experiments performed in NCD-SWEET beamline at ALBA synchrotron (Cerdanyola del Vallès, Barcelona, Spain) with the collaboration of ALBA staff.

References

1 L. Ding, Z.-D. Yu, X.-Y. Wang, Z.-F. Yao, Y. Lu, C.-Y. Yang, J.-Y. Wang and J. Pei, *Chem. Rev.*, 2023, **123**, 7421–7497.
2 X. Guo and A. Facchetti, *Nat. Mater.*, 2020, **19**, 922–928.
3 A. J. Heeger, *Chem. Soc. Rev.*, 2010, **39**, 2354–2371.
4 K. Liu, B. Ouyang, X. Guo, Y. Guo and Y. Liu, *npj Flexible Electron.*, 2022, **6**, 1.
5 M. Karl, J. M. E. Glackin, M. Schubert, N. M. Kronenberg, G. A. Turnbull, I. D. W. Samuel and M. C. Gather, *Nat. Commun.*, 2018, **9**, 1525.
6 U. Lange, N. V. Roznyatovskaya and V. M. Mirsky, *Anal. Chim. Acta*, 2008, **614**, 1–26.
7 W. Li, M. Liang, J. Qi and D. Ding, *Macromol. Rapid Commun.*, 2023, **44**, 2300496.
8 Y. Liu, P. Bhattarai, Z. Dai and X. Chen, *Chem. Soc. Rev.*, 2019, **48**, 2053–2108.
9 Y. Cai, Z. Wei, C. Song, C. Tang, W. Han and X. Dong, *Chem. Soc. Rev.*, 2019, **48**, 22–37.
10 G. Li, V. Shrotriya, J. Huang, Y. Yao, T. Moriarty, K. Emery and Y. Yang, *Nat. Mater.*, 2005, **4**, 864–868.
11 C. J. Brabec, M. Heeney, I. McCulloch and J. Nelson, *Chem. Soc. Rev.*, 2011, **40**, 1185–1199.
12 D. Yang, Z. Li, Z. Li, X. Zhao, T. Zhang, F. Wu, Y. Tian, F. Ye, Z. Sun and X. Yang, *Polym. Chem.*, 2017, **8**, 4332–4338.
13 S. Marina, E. Gutierrez-Fernandez, J. Gutierrez, M. Gobbi, N. Ramos, E. Solano, J. Rech, W. You, L. Hueso, A. Tercjak, H. Ade and J. Martin, *Mater. Horiz.*, 2022, **9**, 1196–1206.
14 S. X. Drakopoulos, J. Cui, M. Asandulesa, P. W. M. Blom, A. Nogales and K. Asadi, *Macromolecules*, 2024, **57**, 2661–2668.
15 S. Ulum, N. Holmes, D. Darwis, K. Burke, A. L. David Kilcoyne, X. Zhou, W. Belcher and P. Dastoor, *Sol. Energy Mater. Sol. Cells*, 2013, **110**, 43–48.
16 P. Ramar, B. V. Aishwarya and D. Samanta, *Chem. Commun.*, 2021, **57**, 12964–12967.
17 X. Wang, K. Maeda, A. Thomas, K. Takanabe, G. Xin, J. M. Carlsson, K. Domen and M. Antonietti, *Nat. Mater.*, 2009, **8**, 76–80.
18 T. Watanabe, A. Kitamura, E. Kojima, C. Nakayama, K. Hashimoto, A. Fujishima, D. Ollis and H. Al-Ekabi, *Photocatalytic purification and treatment of water and air*, Elsevier, Amsterdam, 1993, p. 747.
19 M. Criado-Gonzalez, C. Marzuoli, L. Bondi, E. Gutierrez-Fernandez, G. Tullii, P. Lagonegro, O. Sanz, T. Cramer, M. R. Antognazza and D. Mecerreyes, *Nano Lett.*, 2024, **24**, 7244–7251.
20 M. Zangoli, A. Cantelli, A. Candini, A. Lewinska, F. Fardella, A. Tino, G. Tommasini, M. Wnuk, M. Moschetta, S. Perotto, M. Lucarini, C. Tortiglione, G. Lanzani and F. Di Maria, *J. Phys. Chem. C*, 2023, **127**, 4672–4683.
21 J. Schneider, M. Matsuoka, M. Takeuchi, J. Zhang, Y. Horiuchi, M. Anpo and D. W. Bahnemann, *Chem. Rev.*, 2014, **114**, 9919–9986.
22 C. B. Anucha, I. Altin, E. Bacaksiz and V. N. Stathopoulos, *Chem. Eng. J. Adv.*, 2022, **10**, 100262.
23 M. A. Oturan and J.-J. Aaron, *Crit. Rev. Environ. Sci. Technol.*, 2014, **44**, 2577–2641.
24 C. Byrne, G. Subramanian and S. C. Pillai, *J. Environ. Chem. Eng.*, 2018, **6**, 3531–3555.
25 M. F. Hanafi and N. Sapawe, *Mater. Today: Proc.*, 2020, **31**, A141–A150.

26 H. Kumari, S. Suman, R. Ranga, S. Chahal, S. Devi, S. Sharma, S. Kumar, P. Kumar, S. Kumar, A. Kumar and R. Parmar, *Water, Air, Soil Pollut.*, 2023, **234**, 349.
27 S. Water, Hygiene and Health (WSH) Team, *Progress on household drinking water, sanitation and hygiene* 2000–2020*: Five years into the SDGs*, Report 978 92 4 003084 8, 2020.
28 X. Xu, S. Ozden, N. Bizmark, C. B. Arnold, S. S. Datta and R. D. Priestley, *Adv. Mater.*, 2021, **33**, 2007833.
29 H. Zhu, L. Gong and Z. Li, *Appl. Surf. Sci.*, 2020, **505**, 144639.
30 H. Hintz, H. J. Egelhaaf, L. Lüer, J. Hauch, H. Peisert and T. Chassé, *Chem. Mater.*, 2011, **23**, 145–154.
31 M. Manceau, A. Rivaton, J.-L. Gardette, S. Guillerez and N. Lemaître, *Polym. Degrad. Stab.*, 2009, **94**, 898–907.
32 K. Landfester, R. Montenegro, U. Scherf, R. Güntner, U. Asawapirom, S. Patil, D. Neher and T. Kietzke, *Adv. Mater.*, 2002, **14**, 651–655.
33 G. Nagarjuna, M. Baghgar, J. A. Labastide, D. D. Algaier, M. D. Barnes and D. Venkataraman, *ACS Nano*, 2012, **6**, 10750–10758.
34 E. Gutiérrez-Fernández, T. A. Ezquerra, E. Rebollar, J. Cui, S. Marina, J. Martín and A. Nogales, *Polymer*, 2021, **218**, 123515.
35 L. E. Brus, *J. Chem. Phys.*, 1984, **80**, 4403–4409.
36 S. Ghosh, S. Chakraborty, A. Ghosh, K. Marjit, G. Ghosh and A. Patra, *J. Phys. Chem. C*, 2022, **126**, 18177–18187.
37 Y. Jin, F. Ye, M. Zeigler, C. Wu and D. T. Chiu, *ACS Nano*, 2011, **5**, 1468–1475.
38 J. A. Labastide, M. Baghgar, I. Dujovne, B. H. Venkatraman, D. C. Ramsdell, D. Venkataraman and M. D. Barnes, *J. Phys. Chem. Lett.*, 2011, **2**, 2089–2093.
39 P. Parkinson, C. Müller, N. Stingelin, M. B. Johnston and L. M. Herz, *J. Phys. Chem. Lett.*, 2010, **1**, 2788–2792.
40 M. Sawicki, *Publ. Astron. Soc. Pac.*, 2012, **124**, 1208.
41 G. Ashiotis, A. Deschildre, Z. Nawaz, J. P. Wright, D. Karkoulis, F. E. Picca and J. Kieffer, *J. Appl. Crystallogr.*, 2015, **48**, 510–519.
42 J. Clark, C. Silva, R. H. Friend and F. C. Spano, *Phys. Rev. Lett.*, 2007, **98**, 206406.
43 F. C. Spano and C. Silva, *Annu. Rev. Phys. Chem.*, 2014, **65**, 477–500.
44 J. Tauc, R. Grigorovici and A. Vancu, *Phys. Status Solidi B*, 1966, **15**, 627–637.
45 B. Ferreira, P. F. da Silva, J. S. Seixas de Melo, J. Pina and A. Maçanita, *J. Phys. Chem. B*, 2012, **116**, 2347–2355.
46 N. Banerji, S. Cowan, E. Vauthey and A. J. Heeger, *J. Phys. Chem. C*, 2011, **115**, 9726–9739.
47 S. Cook, A. Furube and R. Katoh, *Energy Environ. Sci.*, 2008, **1**, 294–299.
48 N. Banerji, S. Cowan, M. Leclerc, E. Vauthey and A. J. Heeger, *J. Am. Chem. Soc.*, 2010, **132**, 17459–17470.
49 S. Bellani, D. Fazzi, P. Bruno, E. Giussani, E. V. Canesi, G. Lanzani and M. R. Antognazza, *J. Phys. Chem. C*, 2014, **118**, 6291–6299.
50 E. Mosconi, P. Salvatori, M. I. Saba, A. Mattoni, S. Bellani, F. Bruni, B. Santiago-Gonzalez, M. R. Antognazza, S. Brovelli, G. Lanzani, H. Li, J.-L. Brédas and F. De Angelis, *ACS Energy Lett.*, 2016, **1**, 454–463.
51 A. Mills and J. Wang, *J. Photochem. Photobiol., A*, 1999, **127**, 123–134.
52 M. A. Rauf, M. A. Meetani, A. Khaleel and A. Ahmed, *Chem. Eng. J.*, 2010, **157**, 373–378.
53 A. Krosuri, S. Wu, M. A. Bashir and M. Walquist, *J. Water Process Eng.*, 2021, **40**, 101926.